# Imaging the Renner–Teller effect using laser-induced electron diffraction

Kasra Amini[a,b,1], Michele Sclafani[a,1], Tobias Steinle[a,1], Anh-Thu Le[c,2], Aurelien Sanchez[a], Carolin Müller[d], Johannes Steinmetzer[d], Lun Yue[d], José Ramón Martínez Saavedra[a], Michaël Hemmer[a], Maciej Lewenstein[a,e], Robert Moshammer[f], Thomas Pfeifer[f], Michael G. Pullen[a], Joachim Ullrich[f,g], Benjamin Wolter[a], Robert Moszynski[b], F. Javier García de Abajo[a,e], C. D. Lin[c], Stefanie Gräfe[d,h], and Jens Biegert[a,e,3]

[a]ICFO–Institut de Ciencies Fotoniques, The Barcelona Institute of Science and Technology, 08860 Castelldefels (Barcelona), Spain; [b]Department of Chemistry, University of Warsaw, 02-093 Warsaw, Poland; [c]Department of Physics, J. R. Macdonald Laboratory, Kansas State University, Manhattan, KS 66506-2604; [d]Institute of Physical Chemistry, Friedrich-Schiller University, 07743 Jena, Germany; [e]ICREA, 08010 Barcelona, Spain; [f]Max-Planck-Institut für Kernphysik, 69117 Heidelberg, Germany; [g]Physikalisch-Technische Bundesanstalt, D-38116 Braunschweig, Germany; and [h]Abbe Center of Photonics, Friedrich-Schiller University, 07745 Jena, Germany

Edited by Shaul Mukamel, University of California, Irvine, CA, and approved March 8, 2019 (received for review October 10, 2018)

**Structural information on electronically excited neutral molecules can be indirectly retrieved, largely through pump–probe and rotational spectroscopy measurements with the aid of calculations. Here, we demonstrate the direct structural retrieval of neutral carbonyl disulfide ($CS_2$) in the $\tilde{B}^1B_2$ excited electronic state using laser-induced electron diffraction (LIED). We unambiguously identify the ultrafast symmetric stretching and bending of the field-dressed neutral $CS_2$ molecule with combined picometer and attosecond resolution using intrapulse pump–probe excitation and measurement. We invoke the Renner–Teller effect to populate the $\tilde{B}^1B_2$ excited state in neutral $CS_2$, leading to bending and stretching of the molecule. Our results demonstrate the sensitivity of LIED in retrieving the geometric structure of $CS_2$, which is known to appear as a two-center scatterer.**

structural dynamics | electron diffraction | attosecond wave packet | laser-induced electron diffraction | nonadiabatic dynamics

Many important phenomena in biology, chemistry, and physics can be described only beyond the Born–Oppenheimer (BO) approximation, giving rise to nonadiabatic dynamics and the coupling of nuclear (vibrational and rotational) and electronic motion in molecules (1–7). One prominent example where the BO approximation breaks down is the Renner–Teller effect (8, 9): In any highly symmetric linear molecule with symmetry-induced degeneracy of electronic states, nonadiabatic coupling of (vibrational) nuclear and electronic degrees of freedom can lead to the distortion of the nuclear framework on a timescale comparable with electronic motion. The system's symmetry is then reduced by the bending of the molecule to split the degenerate electronic state into two distinct potential energy surfaces (PESs), leading to a more stable, bent conformer.

Here, we demonstrate the direct imaging of Renner–Teller nonadiabatic vibronic dynamics in neutral carbonyl disulfide ($CS_2$) with combined picometer and attosecond resolution through intrapulse pump–probe excitation and measurement with laser-induced electron diffraction (LIED) (10–16). Our results shed light on the vibronic excitation of a neutral linear molecule in the rising edge of our laser field that causes bending and stretching of the molecule. High-momentum transfers experienced by the electron wave packet (EWP) ($U_p = 85$ eV) with large scattering angles enable the electron to penetrate deep into the atomic cores, allowing us to resolve a strongly symmetrically stretched and bent $CS_2$ molecule most likely in the $\tilde{B}^1B_2$ excited electronic state.

Specifically, we pump and probe $CS_2$ molecules in a one-pulse LIED measurement to capture a single high-resolution snapshot of the molecular structure at around the peak of the strong laser field. By analyzing the angular dependence of the experimentally detected molecular interference signal, we directly retrieve a symmetrically stretched and bent $CS_2^+$ structure. We subsequently present results from state-of-the-art quantum dynamical calculations to investigate the mechanism behind the linear-to-bent transition that occurs in field-dressed $CS_2$.

## Molecular Structure Extraction

Fig. 1 displays the results for three different electron returning energies, $E_R = 160$ eV, 170 eV, and 180 eV. From the measured momentum distribution, shown in Fig. 1*A*, the molecular differential cross-section (DCS) weighted by the molecular ionization rate and the alignment distribution is extracted using the quantitative rescattering (QRS) theory (*SI Appendix*). Molecular structural information is then obtained from the field-free molecular DCS via the molecular contrast factor (MCF). Fig. 1*B* shows the experimental MCF (black circles) and the theoretical MCFs corresponding to the equilibrium geometric structure of the $\tilde{X}^1\Sigma_g^+$ electronic ground state (orange trace) (9), the quasi-linear geometry (green trace) (17, 18), and the geometric structure that theoretically agrees best with the experimentally measured structure (red trace). Overall, there is a good fit

## Significance

**Laser-induced electron diffraction is a molecular-scale electron microscopy that captures clean snapshots of a molecule's geometry with subatomic picometer and attosecond spatiotemporal resolution. We induce and unambiguously identify the stretching and bending of a linear triatomic molecule following the excitation of the molecule to an excited electronic state with a bent and stretched geometry. We show that we can directly retrieve the structure of electronically excited molecules that is otherwise possible through indirect retrieval methods such as pump–probe and rotational spectroscopy measurements.**

Author contributions: J.B. designed research; K.A., M.S., T.S., A.-T.L., A.S., C.M., J.S., L.Y., J.R.M.S., M.H., M.L., R. Moshammer, M.G.P., J.U., B.W., and J.B. performed research; A.-T.L., C.M., J.S., L.Y., J.R.M.S., R. Moszynski, F.J.G.d.A., C.D.L., and S.G. contributed new reagents/analytic tools; K.A., M.S., T.S., A.S., and M.G.P. analyzed data; and K.A., M.S., T.S., A.-T.L., M.L., R. Moshammer, T.P., J.U., R. Moszynski, F.J.G.d.A., C.D.L., S.G., and J.B. wrote the paper.

The authors declare no conflict of interest.

This article is a PNAS Direct Submission.



[1]K.A., M.S., and T.S. contributed equally to this work.

[2]Present address: Department of Physics, Missouri University of Science and Technology, Rolla, MO 65409.

[3]To whom correspondence should be addressed. Email: jens.biegert@icfo.eu.

This article contains supporting information online at www.pnas.org/lookup/suppl/doi:10.1073/pnas.1817465116/-/DCSupplemental.

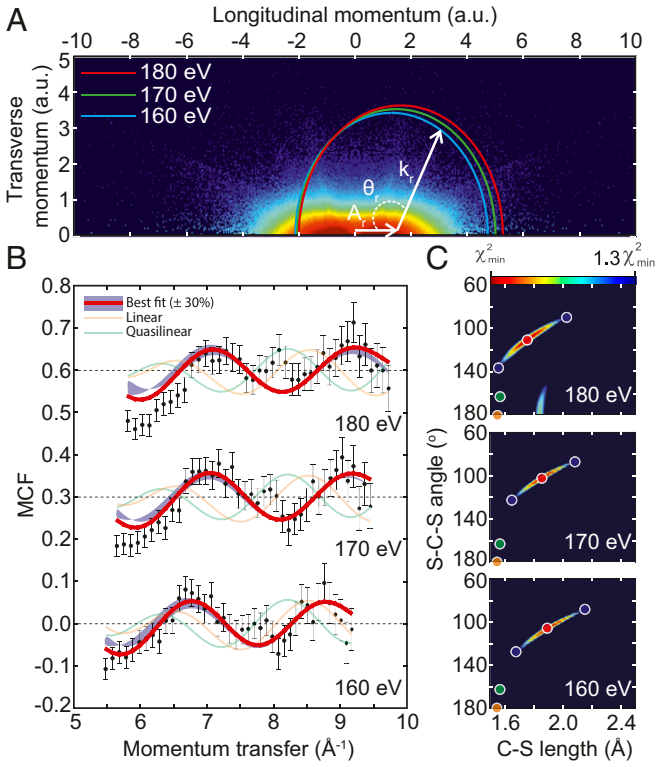


**Fig. 1.** LIED imaging of laser-induced skeletal deformations in $CS_2$. (*A*) Double differential cross-sections are extracted by integrating the experimental momentum distribution map along the rescattering angle, $\theta_r$, of the circle defined by the parametric relations $p_{long} = -A_r \pm (k_r \times \cos\theta_r)$ and $p_{trans} = k_r \times \sin\theta_r$, where $A_r$ is the value of the field vector at the time of rescattering. (*B*) Comparison of the experimental (black circles) molecular contrast factor (MCF) to the theoretical MCFs associated with the equilibrium geometric structure of the $\tilde{X}^1\Sigma_g^+$ electronic ground state (orange trace) (9), the quasilinear geometry (green trace) (17, 18), and the geometric structure that theoretically agrees best with the experimentally measured structure (red trace). The blue shaded region illustrates the sensitivity of the theoretical MCFs when varying $R_{CS}$ and $\Phi_{SCS}$ by around ±0.25 Å and ±20°, respectively, corresponding to a 30% increase from the $\chi^2$ minimum (*SI Appendix*). The data shown correspond to rescattered electrons with kinetic energies of 160 eV, 170 eV, and 180 eV. (*C*) $CS_2$ structural parameters are retrieved by locating the minimum of the $\chi^2$ map (*SI Appendix*, Eq. **S1**). Here, the most probable $CS_2$ geometry (red circle in each plot) is shown along with a 30% variation of the $\chi^2$ minimum (blue circles). The orange circle indicates the equilibrium geometry of neutral $CS_2$ in its $\tilde{X}^1\Sigma_g^+$ ground electronic state (1.55 Å, 180°) (9), whereas the green circle corresponds to $CS_2$ in a quasilinear configuration (1.54 Å, 163°) (17, 18).

between the experimental MCF and the theoretical MCF that best fits the experimental data. An additional peak is observed in the experimental data between 7.5 $Å^{-1}$ and 8.0 $Å^{-1}$ in Fig. 1*B* that is not captured by our best-fit single-structure theoretical MCF and is most likely due to a small contribution from another structure. Nevertheless, the single-structure fitting algorithm used in this work already agrees well with the experimental MCFs for a rather broad range of momentum transfer from around 5.5 $Å^{-1}$ to 9.5 $Å^{-1}$, and thus we believe that the extracted bent structure is the dominant one. Retrieving this information at different returning electron kinetic energies yields consistent results with bent and symmetrically stretched neutral $CS_2$, as shown in Fig. 1*C*.

## Bent and Stretched Molecular Structure

The geometric parameters are retrieved from our LIED measurements as a function of the electron returning energy, as shown in Fig. 2. We measure a C-S bond length $R_{CS}$ = 1.86 ± 0.23 Å and an S-C-S angle $\Phi_{SCS}$ = 104.0° ± 20.2°, which correspond to a strongly symmetrically stretched and bent molecule. Since field-free neutral $CS_2$ in the ground electronic state, $\tilde{X}^1\Sigma_g^+$, is linear in geometry ($R_{eq}$ = 1.55 Å and $\Phi_{SCS}$ = 180°) (18), a linear-to-bent transition occurs that leads to the experimentally measured bent LIED structure.

## Quantum Chemistry Dynamical Calculations

We performed advanced, state-of-the-art quantum dynamical calculations of coupled electron–nuclear motions on the field-dressed PESs in the presence of an intense laser field to investigate the mechanism behind such a linear-to-bent transition (*SI Appendix*). Our calculations reveal a Renner–Teller excitation mechanism that leads to the stretching and bending of neutral $CS_2$, with a schematic of the excitation shown in Fig. 3*A*. Optical excitation to the lowest-lying singlet excited electronic states, such as the doubly degenerate $^1\Delta_u$ state, from the $\tilde{X}^1\Sigma_g^+$ ground state in field-free neutral $CS_2$ is strictly dipole forbidden in the linear geometry ($D_{\infty h}$) due to symmetry considerations (gray arrow in Fig. 3*A*). However, in the presence of a strong field, our wave packet calculations in Fig. 4*A* show that the field-dressed (FD) molecule initially bends by ∼10° within 90 fs (blue rectangle in Fig. 4*A*) to split the degeneracy of $^1\Delta_u$ into two bent states ($\tilde{A}^1A_2$ and $\tilde{B}^1B_2$) in neutral $CS_2$. This enables the nuclear wave packet to reach nonequilibrium positions in the initially bent molecule, such that only a transition from the $\tilde{X}^1A_1$ ground state to the $\tilde{B}^1B_2$ excited state becomes dipole allowed (black arrow in Fig. 3*A*) in the bent geometry ($C_{2v}$). Our quantum dynamical calculations confirm that symmetric stretching and bending in the laser field occurs, leading to an estimated population of about 3% in the $\tilde{B}^1B_2$ state in neutral $CS_2$. Our calculations for neutral $CS_2$ in Fig. 4*A* show that the molecule in the excited state bends up to about 120° at $t$ = 0 fs (i.e., near the maximum of the pulse envelope; red oval in Fig. 4*A*). The wave packet in the $\tilde{B}^1B_2$ state then proceeds to find its lowest-energy equilibrium position ($R_{eq}$ = 1.64 Å and $\Phi_{SCS}$ = 130°) (16–19), as shown in Fig. 3*B*. Other excited electronic states are not populated due to small dipole couplings, even in the deformed geometry. Since the energy gap of $\tilde{B}^1B_2$ relative to the ground state is ∼4.5 eV according to our calculations, the strong tunneling

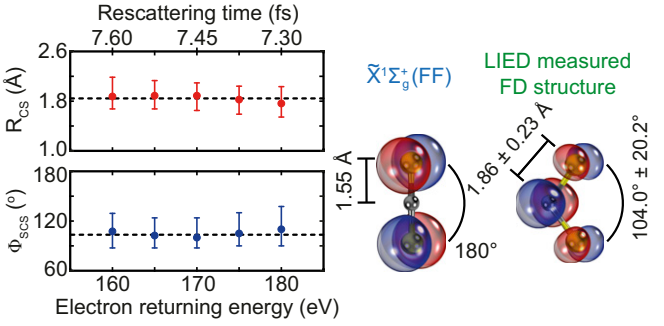


**Fig. 2.** Stretching and bending of field-dressed $CS_2$. Geometrical parameters of $CS_2$ are retrieved as a function of the electron returning energy. By fitting a constant line, we estimate a C-S bond length $R_{CS}$ = 1.86 ± 0.23 Å and a S-C-S angle $\Phi_{SCS}$ = 104.0° ± 20.2°, which correspond to a strongly symmetrically stretched and bent neutral $CS_2$. *Top Left* shows the return time of the rescattered electrons. *Right* shows models with molecular orbitals for field-free (FF) neutral $CS_2$ in the ground electronic state, $\tilde{X}^1\Sigma_g^+$, and the LIED-measured field-dressed (FD) structure. The corresponding $R_{CS}$ and $\Phi_{SCS}$ values for these two structures are indicated.

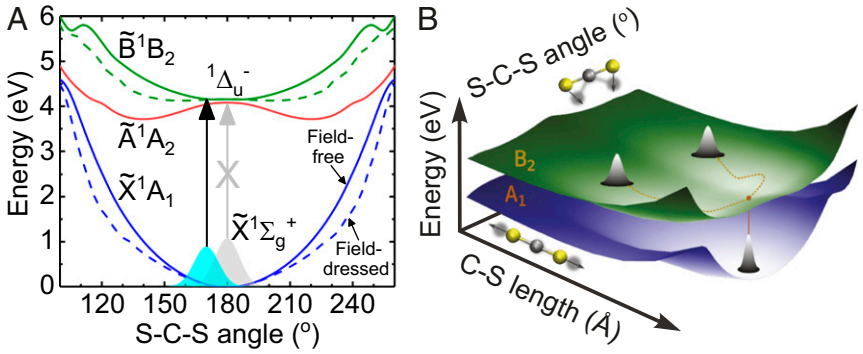


**Fig. 3.** Renner–Teller excitation mechanism in neutral $CS_2$. (*A*) Potential energy curves (PECs) for the field-free (solid curves) neutral $CS_2$ in the ground electronic state along with the $\tilde{X}^1A_1$ (blue), the $\tilde{A}^1A_2$ (red), and the $\tilde{B}^1B_2$ (green) excited electronic states are shown as a function of the S-C-S angle at fixed $R_{CS}$ = 1.86 Å. The corresponding field-dressed (dashed curves) PECs are also shown. In the linear geometry ($D_{\infty h}$), a transition from the $\tilde{X}^1\Sigma_g^+$ ground electronic state to the $^1\Delta_u$ excited electronic state is dipole forbidden (gray vertical arrow) due to symmetry considerations. However, our calculations show that the molecule begins to bend by 10° ($C_{2v}$) in the presence of a strong field. At the same time, at bent geometries, the twofold degeneracy of $^1\Delta_u$ is lifted and splits into two distinct bent excited electronic states: $\tilde{A}^1A_2$ and $\tilde{B}^1B_2$. At these bent geometries, a transition from the $\tilde{X}^1A_1$ ground state to the $\tilde{B}^1B_2$ excited state becomes dipole allowed (black vertical arrow). (*B*) Potential energy surfaces (PESs) of field-dressed (FD) $CS_2$ in the $\tilde{X}^1A_1$ ground electronic state and the $\tilde{B}^1B_2$ excited state. Once the $\tilde{B}^1B_2$ state is populated, the nuclear wave packet evolves toward the equilibrium position of the $\tilde{B}^1B_2$ state.

ionization from $\tilde{B}^1B_2$ completely dominates, which permits the identification of the $\tilde{B}^1B_2$ state. Moreover, our dynamical calculations also show that the geometry of the cation (1.74 Å, 102°) does not change significantly relative to the deformed excited neutral (1.70 Å, 117°) within half a laser cycle after tunnel ionization from the $\tilde{B}^1B_2$ state (i.e., during the 7- to 8-fs excursion time of the rescattering electron; green oval in Fig. 4*B*).

The exact geometry of neutral $CS_2$ in the $\tilde{B}^1B_2$ excited electronic state is still discussed (19, 20); spectroscopic measurements by Jungen et al. (17) reported a quasilinear structure (1.544 ± 0.006 Å, 163°), while a much more recent analysis of the rotational progressions in the $\tilde{B}^1B_2 \leftarrow \tilde{X}^1\Sigma_g^+$ spectrum led to a largely corrected, significantly bent geometry (1.64 Å, 131.9°) (21). These measurements in fact indirectly retrieve structural information. Our directly measured structure (1.86 ± 0.23 Å, 104.0° ± 20.2°) is in general agreement with previous theoretical investigations (~1.64 Å, ~130°) (18–20) into neutral $CS_2$ in the $\tilde{B}^1B_2$ excited state. The MCF that corresponds to the quasilinear geometry previously measured (1.544 ± 0.006 Å, 163°) (17) does not agree with our measured data. In contrast, our results clearly support a symmetrically stretched and strongly bent molecular structure. Analogous observations of $CS_2$ skeletal deformation have been recently reported by Yang et al. (22), who imaged an increase in $R_{CS}$ by 0.16 Å and 0.20 Å with respect to the equilibrium bond length when a 60-fs, 800-nm laser pulse is increased in intensity from $1.3\times10^{13}$ $Wcm^{-2}$ to $2.4\times10^{13}$ $Wcm^{-2}$, respectively. An assumed linear extrapolation of their results would produce a 0.43-Å bond length increase for the intensity we use ($9\times10^{13}$ $Wcm^{-2}$), which is fully consistent with the value reported here of 0.31 ± 0.23 Å. This corresponds to strongly symmetrically stretched C-S bonds in vibronically excited neutral $CS_2$. Although clear indications of symmetric bond elongation were observed by Yang et al. (22), no firm conclusion was drawn about the bending vibration because of the limited spatial resolution (1.2 Å) of their ultrafast electron diffraction (UED) probe, due to the small momentum transfer of their scattered electrons (<3.5 $Å^{-1}$). It should also be noted that Yang et al. (22) used a field-free probe of molecular structure through UED with an ~400-fs pulse duration. Moreover, the lack of an electron–ion coincidence-based detection scheme added further ambiguity to the physical mechanism behind

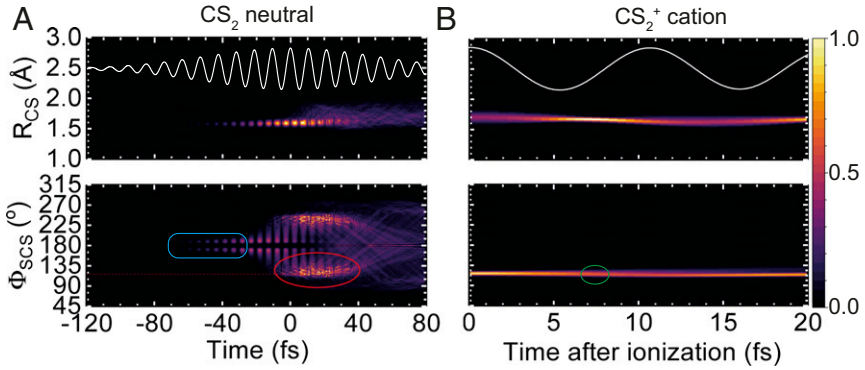


**Fig. 4.** Quantum dynamical wave packet calculations. (*A* and *B*) The stretching (*Top*) of C-S internuclear distance, $R_{CS}$, and bending (*Bottom*) of the S-C-S bond angle, $\phi_{SCS}$, for (*A*) neutral $CS_2$ in the $\tilde{B}^1B_2$ state and (*B*) $CS_2^+$ cation. The starting conditions used are (*A*) neutral $CS_2$ in the $\tilde{X}^1\Sigma_g^+$ ground electronic state (1.55 Å, 180°) and (*B*) neutral $CS_2$ in the $\tilde{B}^1B_2$ excited electronic state (1.7 Å, 117°). The blue rectangle indicates the initial bending of neutral $CS_2$. The red (green) oval indicates the relevant structure at around the time of ionization (rescattering), $t_i$ ($t_r$). Here, molecules are 90° to the laser polarization. In *A*, $t$ = 0 fs corresponds to the peak of the 85-fs (FWHM) 3.1-μm pulse envelope, while in *B* the time axis corresponds to the time after ionization. The corresponding laser field is shown as white traces in *A* and *B*, *Top*.

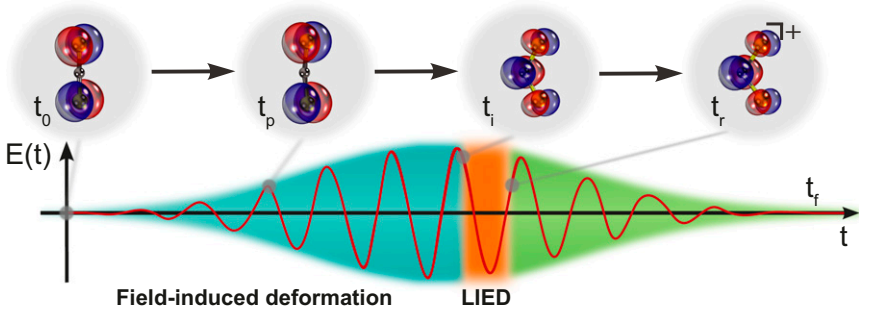


**Fig. 5.** Illustration of field-induced deformation and LIED measurement. In our LIED measurement, the neutral $CS_2$ molecule is first symmetrically stretched and initially bent by 10° (at time $t_p$) before leading to the significantly bent $CS_2$ structure at the time of ionization, $t_i$. A high-resolution snapshot is recorded by the high-energy electrons at the point of rescattering, $t_r$.

the IR-induced excitation, with two possible mechanisms suggested by the authors: excitation of an electronic state through a multiphoton process and formation of ions with longer bond lengths.

We use LIED to directly retrieve the geometric transformation of neutral $CS_2$ due to the Renner–Teller effect. Our measurements unambiguously identify a bent and symmetrically stretched $CS_2$ molecule ($R_{CS}$ = 1.86 ± 0.23 Å, $\Phi_{SCS}$ = 104.0° ± 20.2°) that is most likely populating the $\tilde{B}^1B_2$ excited electronic state. This finding is also supported by our state-of-the-art quantum dynamical ab initio molecular dynamics calculations, which describe the linear-to-bent $\tilde{B}^1B_2 \leftarrow \tilde{X}^1\Sigma_g^+$ transition in neutral $CS_2$. Moreover, previous theory and indirect measurements of neutral $CS_2$ in the $\tilde{B}^1B_2$ excited state also broadly support our LIED measurement and calculations (18–21).

We find that the nuclear distortion in fact first proceeds through the stretching of the C-S bonds before the molecule departs from the linear geometry and begins to bend on the rising edge of the LIED pulse (at time $t_p$ in Fig. 5). Consequently, a bent neutral $CS_2$ molecule most likely in the $\tilde{B}^1B_2$ excited electronic state is preferentially subsequently ionized at the peak of the pulse (at time $t_i$ in Fig. 5) to initiate the LIED process. LIED is the elastic rescattering of the highly energetic returning EWP onto the molecular ion (at time $t_r$ in Fig. 5), with structural information embedded within the rescattered EWP's momentum distribution at the time of recollision (*Methods*) (12, 14, 23). Here, the returning EWP scatters against the $CS_2^+$ molecular ion (at time $t_r$), which has a similar strongly stretched and bent geometry to that of the neutral $CS_2$ in an excited electronic state at the point of ionization (at time $t_i$ in Fig. 5). However, during the excursion time of the returning electron of about 7–8 fs, vibrational dynamics on the cationic potential energy curves in the presence of the laser field occur. During that time, as our calculations show (green oval in Fig. 4*B*), the excited cation bends slightly farther, leading to a structure that is in good agreement with the experimentally observed bent and stretched structure.

Ultimately, our results illustrate the utility of intrapulse LIED to retrieve structural transformation with combined picometer and attosecond resolution, allowing us to directly visualize nonadiabatic dynamics in molecular systems.

## Methods

**Mid-IR Optical Parametric Chirped Pulse Amplifier Source.** A home-built optical parametric chirped pulse amplifier (OPCPA) setup generates 85-fs, 3.1-μm pulses at a 160-kHz repetition rate with up to 21 W output power (24, 25). The OPCPA system is seeded by a passively carrier-envelope-phase (CEP) stable frequency comb generated by the difference frequency of a dual-color fiber laser system (26). The mid-IR wavelength of 3.1 μm ensures that the target is strong-field ionized in the tunneling regime. The laser pulse is focused to a spot size of 6–7 μm, resulting in a peak intensity of $9 \times 10^{13}$ $Wcm^{-2}$.

**Reaction Microscope Detection System.** The experimental setup is based on a reaction microscope (ReMi) which has been previously described in detail in refs. 27–29. Briefly, a doubly skimmed supersonic jet of carbon disulfide provides the cold molecular target with a rotational temperature of <100 K. Homogeneous electric and magnetic extraction fields are employed to guide the ionic fragments and the corresponding electrons to separate detectors in the ReMi. Each detector consists of delay line detectors (Roentdek) which record the full 3D momenta of charged particles from a single molecular fragmentation event in full electron–ion coincidence. In all experiments, the laser polarization is aligned perpendicular to the spectrometer axis, parallel to the jet.

**Molecular Structure Extraction.** Structural information of the molecular sample is retrieved from the electron momentum distribution within the frame of the QRS theory and the independent atomic-rescattering model (IAM) (30–32). We extracted the molecular DCS from the experimental photoelectron momentum distribution as previously described in ref. 14. See *SI Appendix* for further details.

**ACKNOWLEDGMENTS.** We thank A. Stolow and J. Küpper for helpful and inspiring discussions. We acknowledge financial support from the Spanish Ministry of Economy and Competitiveness (MINECO), through the "Severo Ochoa" Programme for Centres of Excellence in R&D (SEV-2015-0522) Fundació Cellex Barcelona and the Centres de Recerca de Catalunya (CERCA) Programme/Generalitat de Catalunya. K.A., M.S., T.S., A.S., M.H., M.G.P., B.W., and J.B. acknowledge the European Research Council (ERC) for ERC Advanced Grant TRANSFORMER (788218), MINECO for Plan Nacional FIS2017-89536-P, Agència de Gestió d'Ajuts Universitaris i de Recerca for 2017 SGR1639, and Laserlab-Europe (EU-H2020 654148). K.A., J.B., M.L., and R. Moszynski acknowledge the Polish National Science Center within the project Symfonia, 2016/20/W/ST4/00314. A.S. and J.B. acknowledge Marie Sklodowska-Curie Grant Agreement 641272. F.J.G.d.A. acknowledges help from MINECO (MAT2017-88492-R) and the ERC (Advanced Grant 789104-eNANO). C.M. and S.G. acknowledge the ERC Consolidator Grant QUEMCHEM (772676). L.Y. and S.G. acknowledge funding from the German Research Foundation, Grant GR 4482/2. A.-T.L. and C.D.L. are supported by the US Department of Energy under Grant DE-FG02-86ER13491. M.L. acknowledges support from the Ministerio de Economía y Competitividad through Plan Nacional (Grant FIS2016-79508-P FISICATEAMO), de Catalunya (Grant SGR 1341), the CERCA Programme, the ERC (Advanced Grant OSYRIS), and the European Union's Horizon 2020 research and innovation programme FETPRO QUIC (Grant 641122).

1. Yang J, et al. (2018) Imaging $CF_3I$ conical intersection and photodissociation dynamics with ultrafast electron diffraction. *Science* 361:64–67.
2. Attar AR, et al. (2017) Femtosecond x-ray spectroscopy of an electrocyclic ring-opening reaction. *Science* 356:54–59.
3. Worth GA, Cederbaum LS (2004) Beyond Born-Oppenheimer: Molecular dynamics through a conical intersection. *Annu Rev Phys Chem* 55:127–158.
4. Barbatti M, et al. (2010) Relaxation mechanisms of UV-photoexcited DNA and RNA nucleobases. *Proc Natl Acad Sci USA* 107:21453–21458.
5. Kleinermanns K, Nachtigallová D, de Vries MS (2013) Excited state dynamics of DNA bases. *Int Rev Phys Chem* 32:308–342.
6. Bellshaw D, et al. (2017) Ab-initio surface hopping and multiphoton ionisation study of the photodissociation dynamics of $CS_2$. *Chem Phys Lett* 683:383–388.

7. Wang K, McKoy V, Hockett P, Stolow A, Schuurman MS (2017) Monitoring nonadiabatic dynamics in $CS_2$ with time- and energy-resolved photoelectron spectra of wavepackets. *Chem Phys Lett* 683:579–585.
8. Renner R (1934) Zur Theorie der Wechselwirkung zwischen Elektronen- und Kernbewegung bei dreiatomigen, stabförmigen Molekülen [On the theory of the interaction between electronic and nuclear motion in tri-atomic rod-shaped molecules]. *Z Phys* 92:172–193. German.
9. Herzberg G (1966) Molecular spectra and molecular structure: III. *Electronic Spectra and Electronic Structure of Polyatomic Molecules* (D. Van Nostrand Company, Inc., Princeton, NJ), Vol 1.
10. Meckel M, et al. (2008) Laser-induced electron tunneling and diffraction. *Science* 320: 1478–1482.
11. Okunishi M, Niikura H, Lucchese RR, Morishita T, Ueda K (2011) Extracting electron-ion differential scattering cross sections for partially aligned molecules by laser-induced rescattering photoelectron spectroscopy. *Phys Rev Lett* 106:063001.
12. Blaga CI, et al. (2012) Imaging ultrafast molecular dynamics with laser-induced electron diffraction. *Nature* 483:194–197.
13. Xu J, et al. (2014) Diffraction using laser-driven broadband electron wave packets. *Nat Commun* 5:4635.
14. Pullen MG, et al. (2015) Imaging an aligned polyatomic molecule with laser-induced electron diffraction. *Nat Commun* 6:7262.
15. Pullen MG, et al. (2016) Influence of orbital symmetry on diffraction imaging with rescattering electron wave packets. *Nat Commun* 7:11922.
16. Wolter B, et al. (2016) Ultrafast electron diffraction imaging of bond breaking in di-ionized acetylene. *Science* 354:308–312.
17. Jungen C, Malm D, Merer A (1973) Analysis of a $^1\Delta_u$–$^1\Sigma^+_g$ transition of $CS_2$ in the near ultraviolet. *Can J Phys* 51:1471–1490.
18. Zhang Q, Vaccaro PH (1995) Ab initio studies of electronically excited carbon disulfide. *J Phys Chem* 99:1799–1813.
19. Wiberg KB, Wang Y-G, de Oliveira AE, Perera SA, Vaccaro PH (2005) Comparison of CIS- and EOM-CCSD-calculated adiabatic excited-state structures. Changes in charge density on going to adiabatic excited states. *J Phys Chem A* 109:466–477.
20. Brown ST, Van Huis TJ, Hoffman BC, Schaefer HF, III (1999) Excited electronic states of carbon disulphide. *Mol Phys* 96:693–704.
21. Brasen G, Leidecker M, Demtröder W, Shimamoto T, Kato H (1998) New vibrational analysis of the $^1B_2$ ($^1\Delta_u$) state of $CS_2$. *J Chem Phys* 109:2779–2790.
22. Yang J, Beck J, Uiterwaal CJ, Centurion M (2015) Imaging of alignment and structural changes of carbon disulfide molecules using ultrafast electron diffraction. *Nat Commun* 6:8172.
23. Zuo T, Bandrauk A, Corkum PB (1996) Laser-induced electron diffraction: A new tool for probing ultrafast molecular dynamics. *Chem Phys Lett* 259:313–320.
24. Baudisch M, Wolter B, Pullen M, Hemmer M, Biegert J (2016) High power multi-color OPCPA source with simultaneous femtosecond deep-UV to mid-IR outputs. *Opt Lett* 41:3583–3586.
25. Elu U, et al. (2017) High average power and single-cycle pulses from a mid-IR optical parametric chirped pulse amplifier. *Optica* 4:1024–1029.
26. Thai A, Hemmer M, Bates PK, Chalus O, Biegert J (2011) Sub-250-mrad, passively carrier-envelope-phase-stable mid-infrared OPCPA source at high repetition rate. *Opt Lett* 36:3918–3920.
27. Moshammer R, Unverzagt M, Schmitt W, Ullrich J, Schmidt-Böcking H (1996) A $4\pi$ recoil-ion electron momentum analyzer: A high-resolution "microscope" for the investigation of the dynamics of atomic, molecular and nuclear reactions. *Nucl Instrum Methods Phys Res Sect B* 108:425–445.
28. Dörner R, et al. (2000) Cold target recoil ion momentum spectroscopy: A 'momentum microscope' to view atomic collision dynamics. *Phys Rep* 330:95–192.
29. Ullrich J, et al. (2003) Recoil-ion and electron momentum spectroscopy: Reaction-microscope. *Rep Prog Phys* 66:1463–1545.
30. Morishita T, Le AT, Chen Z, Lin CD (2008) Accurate retrieval of structural information from laser-induced photoelectron and high-order harmonic spectra by few-cycle laser pulses. *Phys Rev Lett* 100:013903.
31. Chen Z, Le AT, Morishita T, Lin CD (2009) Quantitative rescattering theory for laser-induced high-energy plateau photoelectron spectra. *Phys Rev A* 79:033409.
32. Lin CD, Le AT, Chen Z, Morishita T, Lucchese RR (2010) Strong-field rescattering physics–Self-imaging of a molecule by its own electrons. *J Phys B At Mol Opt Phys* 43:122001.

PNAS
www.pnas.org

# Supplementary Information for

## Imaging the Renner-Teller effect using laser-induced electron diffraction

Kasra Amini, Michele Sclafani, Tobias Steinle, A.T. Le, Aurelien Sanchez, Carolin Müller, Johannes Steinmetzer, Lun Yue, José Ramón Martínez Saavedra, Michaël Hemmer, Maciej Lewenstein, Robert Moshammer, Thomas Pfeifer, Michael G. Pullen, Joachim Ullrich, Benjamin Wolter, Robert Moszynski, F. Javier García de Abajo, C.D. Lin, Stefanie Gräfe, Jens Biegert

Jens Biegert
Email: jens.biegert@icfo.eu

**This PDF file includes:**

## Supplementary Information Text

**A. Experimental Description.** We generate high-energy rescattering electron wave packets by making use of a home-built optical parametric chirped pulse amplifier (OPCPA) set-up that generates 85 fs (FWHM), 3.1 μm pulses at a 160 kHz repetition rate with up to 21 W output power (1, 2). The OPCPA system is seeded by a passively carrier-envelope-phase (CEP) stable frequency comb generated by the difference frequency of a dual-colour fibre laser system (3). The mid-infrared wavelength of 3.1 μm here used ensures that the target is strong-field ionised in the tunneling regime. The laser pulse is focused to a spot size of 6−7 μm (1/$e^2$ waist) resulting in a peak intensity of $9 \times 10^{13}$ Wcm$^{-2}$. At this peak intensity, the Keldysh parameter was $\gamma$ = 0.30 with a ponderomotive energy of $U_p$ = 85 eV. As the average energy of the returning electron wave packet scales quadratically with the driving wavelength, this laser source allows us to generate electrons with maximum classical return and backscattered electron energies of $E_{ret,max} = 3.17U_p \approx 270$ eV and $E_{back,max} = 10U_p \approx 850$ eV, respectively.

We measure the full three-dimensional momentum distribution of the photoelectrons in coincidence with the $CS_2^+$ ion using a reaction microscope (ReMi) - for details, see for example Ref. (4). Briefly, a doubly-skimmed supersonic jet of carbon disulfide provides the cold molecular target with a rotational temperature of <100K. Homogeneous electric and magnetic extraction fields are employed to guide the ionic fragments and the corresponding electrons to separate detectors in the ReMi. Each detector consists of delay line detectors (Roentdek), which record the full three-dimensional momenta of charged particles from a single molecular fragmentation event in full electron-ion coincidence. In all experiments, the laser polarisation is aligned perpendicular to the spectrometer axis, parallel to the jet. A thorough description of the experimental advantages offered by the unique combination of our mid-IR OPCPA with a ReMi to investigate strong-field physics in the quasistatic regime is provided in Ref. (5). Nevertheless, it is worth emphasizing that our electron-ion coincidence experimental setup allows the structural retrieval of neutral $CS_2$ through its cation $CS_2^+$ since the geometrical structure of $CS_2$ to be investigated does not significantly change upon ionization.

**B. Extraction Of Molecular Structure.** Structural information of the molecular sample is retrieved from the electron momentum distribution within the frame of the quantitative rescattering theory (QRS) and the independent atomic-rescattering model (IAM) (6–8). The procedure for molecular structure extraction has been explained in detail previously (9,10), with only a brief discussion given here. Molecular structural information is extracted from our LIED measurement through the best chi-square fit of the experimental molecular contrast factor (MCF), $\gamma^e$, to the theoretical MCF, $\gamma^t$, using

$$\chi^2(R_{CS}, \Phi_{SCS}) = \sum_n \left[\gamma^e(k_r, \theta_{r,n}) - \gamma^t(k_r, \theta_{r,n})\right]^2 \quad \text{(S1)}$$

where ($k_r$, $\theta_r$) represent the momentum and the scattering angle of the rescattered electron in the rescattering frame (see Fig. 1*A*), whilst *n* is the index of the discretized scattering angle.

The theoretical MCF is calculated using the independent atomic-rescattering model (IAM), and is given by

$$\gamma^{t}(k_r, \theta_r) \equiv \frac{\langle I_{tot}\rangle(\theta) - \langle I_A\rangle(\theta_r)}{\langle I_A\rangle(\theta_r)} = \frac{\sum_{i\neq j} f_i f_j^* \int e^{i\vec{q}\cdot\vec{R}_{ij}} N(\Omega_L)\rho(\Omega_L)d\Omega_L}{\sum_i |f_i|^2 \int N(\Omega_L)\rho(\Omega_L)d\Omega_L}. \quad \text{(S2)}$$

Here, $I_{tot}$ is the total scattering cross-section that we measure, and $I_A$ is the incoherent sum of the scaterring cross-sections from all atoms within the molecule, given by

$$\langle I_A\rangle(\theta) = \sum_i |f_i|^2 \int N(\Omega_L)\rho(\Omega_L)d\Omega_L\,, \quad \text{(S3)}$$

where $\Omega_L$ is the alignment angle of the molecule relative to the polarization axis of the laser field, $\rho(\Omega_L)$ is the molecular alignment distribution, $N(\Omega_L)$ is the ionization rate, and $f_i$ is the complex scattering amplitude for the $i^{th}$ atom by the incident electron. Whilst $\langle I_{tot}\rangle(\theta) - \langle I_A\rangle(\theta_r)$ is the molecular interference term, $\langle I_M\rangle(\theta)$. In fact, the phase factor in $\langle I_M\rangle(\theta)$ encodes both the scattering angle of the incident electron, as quantified by the momentum transfer

$$\vec{q} = \vec{k}_r - \vec{k}_{r0},$$

as well as the internuclear distance vector $\vec{R}_{ij} = \vec{R}_i - \vec{R}_j$ between atoms *i* and *j*. Therefore, the MCF provides a sensitive measure of $\vec{R}_{ij}$ in molecules (9, 10).

The experimental MCF is given by

$$\gamma^{e}(k_r, \theta_r) \equiv \frac{\langle I^{e}_{tot}\rangle(\theta_r) - \langle I_A\rangle(\theta_r)}{\langle I_A\rangle(\theta_r)} = \frac{\beta D^{e}(\theta_r) - \langle I_A\rangle(\theta_r)}{\langle I_A\rangle(\theta_r)}, \quad \text{(S5)}$$

and is calculated using the experimentally determined differential cross-section (DCS), $D_e(\theta_r)$, which is weighted by a factor $\beta$ that provides the best fit to the theoretical MCF.

Here, the molecular alignment distribution, $\rho(\Omega_L)$, was assumed to be isotropic. We calculated the ionization rate, $N(\Omega_L)$, using the strong-field approximation (SFA) and the time-dependent density-functional theory (TDDFT) method, and we consider contributions from the highest occupied molecular orbital (HOMO) only. The contribution of lower lying states (HOMO-1 or HOMO-2) is several orders of magnitude smaller than from the HOMO and hence can be neglected (11). Furthermore, non-perturbative TDDFT for 0.8 μm light (12) and our own real-time-real-space TDDFT calculations for 3.1 μm simulations have shown that the ionization of the inner $3\sigma_u$ orbital (HOMO-2) of $CS_2$ only becomes the dominant response to the laser field for intensities larger than $3 \times 10^{15}$ Wcm$^{-2}$ and molecules whose molecular axis is aligned with the field (12). It should also

be noted that we found the MCFs (shown in Fig. 1*B*) to be quite insensitive with respect to small changes in the ionization rates and molecular alignment distribution.

In $CS_2$, the IAM has been shown to yield excellent agreement between experimental and theoretical DCSs for electrons with kinetic energies of 100−200 eV and scattering angles in the 20−135° range (13). In the present measurements, we record rescattered electrons with sufficient statistics in the kinetic energy range of 160−180 eV and an angular interval of 50−120° (*i.e.*, well within the range of validity of the IAM approximation). The MCF has been shown to be a very sensitive metric for imaging the molecular structure of diatomic and small molecules (10,14–16). At a fixed returning energy, the C-S bond length, $R_{CS}$, is sampled in the retrieval procedure from 1.5 Å to 2.5 Å, whereas the S-C-S angle, $\Phi_{SCS}$, is explored from the linear structure ($\Phi_{SCS}$ = 180°) to a strongly bent structure ($\Phi_{SCS}$ = 60°). As shown in Fig. 1*B*, MCFs are used for retrieving $R_{CS}$ and $\Phi_{SCS}$ by comparing the experimental and theoretical MCFs.

The theoretical MCFs providing the best agreement with the experimental data are shown by the red trace in Fig. 1*B*. The MCF associated with the equilibrium geometric structure of the $\widetilde{X}^1\Sigma_g^+$ electronic ground state is also shown (orange). Complete $\chi^2$ maps calculated according to Eq. *S1* are shown in Fig. 1*C*. We measure a C-S bond length $R_{CS}$ = 1.86 $\pm$ 0.23 Å and an S-C-S angle $\Phi_{SCS}$ = 104.0 $\pm$ 20.2°, which correspond to $CS_2$ in the bent geometry in the presence of the intense laser field, as shown in Fig. 2.

**C. TDDFT Calculations.** In order to model the interaction of $CS_2$ with the intense, mid-infrared laser fields, real-time-real-space TDDFT calculations have been performed using the Octopus (17) program package. A cartesian grid has been utilized with an equidistant grid spacing of d$x$ = d$y$ = d$z$ = 0.12 Å. For computational feasibility, the grid size was reduced to a sphere with a radius of 8.47 Å. Afterwards, absorbing boundary conditions were employed in order to avoid grid reflections of the free components of the electron wave function. With this procedure, the molecule is well situated in the grid and direct ionization can be modelled. However, effects due to electron recollision, such as recollisional excitation or ionization, are not included. Due to the large wave packet spreading at these long wavelengths, we expect these effects to be minor. The laser field was modelled by a $sin^2$ envelope with a central wavelength of 3100 nm, a duration of approximately 8 optical cycles FWHM (*i.e.,* 85 fs) and a peak intensity of $9 \times 10^{13}$ Wcm$^{-2}$.

Exchange contributions were described via the LDA_X functional (18, 19), while correlation was modelled by a modified Perdew-Zunger LDA functional (20). LDA is commonly employed to model strong-field interaction with molecules due to its simplicity and lower computational cost. However, self-interactions do not cancel and its asymptotic behavior scales wrongly. We corrected for self-interaction *via* the average density formalism (21). Table *S1* shows the converged ground state eigenenergies with different approaches and functionals. When comparing the eigenenergies calculated with different LDA functionals, the LDA_X by Perdew and Zunger (20) gave the best results compared to

experiment. Our results agree well with similar TDDFT-based results (12). As expected, the Hartree-Fock (HF) energies are overestimates of the experimental values, while the LDA functional in DFT underestimates the ionization potentials substantially due to the known wrong asymptotic behavior originating from the self-interaction (12).

Our TDDFT calculations have been employed in order to get an overview over the excitation and ionization dynamics of $CS_2$ in an intense laser field. We have implemented the calculations of the orbital norms, $\langle \psi_i(t) | \psi_i(t) \rangle$, and auto-correlation functions, $\langle \psi_i(t=0) | \psi_i(t) \rangle$, in the Octopus program suite (17) in order to be able to investigate which Kohn-Sham molecular orbitals interact with the mid-infrared laser pulse depending on the relative orientation of the laser polarization axis to the molecular axis. Calculations have been performed for $\theta$ = 0° and 90°, where $\theta$ is the angle of the laser polarization relative to the molecular axis.

We have performed two different types of calculations, one keeping the nuclei frozen throughout the calculations, and another one with moving nuclei (Ehrenfest dynamics). Our (non-perturbative) TDDFT calculations show that, for the pulse parameters employed in the experiment, mainly the $\pi_g$ (non-bonding orbital, *n*) and $\pi_u$ (bonding orbital) orbitals are depopulated, depending on the orientation (angle $\theta$). This is in agreement with earlier calculations by Bandrauk *et al.* at 800 nm (12).

Additionally, the TDDFT calculations using (classically) moving nuclei within the Ehrenfest approach show that during laser interaction, the system stretches symmetrically and bends (from $R_{CS}$ = 1.56 Å and $\Phi_{SCS}$ = 180° to $R_{CS}$ = 1.64 Å and $\Phi_{SCS}$ = 124.1°, for θ = 90°, see Fig. *S1*). For θ = 0°, also small contributions of an asymmetric stretch dynamics can be gathered from the TDDFT calculations (Fig. *S2*). However, contributions from the asymmetric stretch are minor when taking orientation-averaging into account. From the TDDFT calculations, we thus extract the transition to the first excited state ($n \rightarrow \pi_u^*$) to be the dominant excitation channel, the dynamics of which will be examined in more detail with wave packet methods, as described below.

**D. Quantum Chemistry Calculations.** The singlet electronic ground and excited state potential surfaces, $V_i(R, \Phi)$, as well as the (transition) dipole moments, $\vec{\mu}(R, \Phi)$, of both the neutral $CS_2$ and the cation $CS_2^+$ have been calculated using the OpenMolcas 8.0 program suite (23) at the state-averaged CASSCF(12,10)/cc-pVTZ level of theory[24]. For the neutral molecule, a (12,10) space was chosen, with the active orbitals displayed in Fig. *S3*.

For the cation, the corresponding (11,10) space was chosen. Altogether, the first 10 configuration interaction (CI) roots have been calculated, using $C_1$ symmetry. The molecule is arranged such that at linear geometries the molecular axis is the $y$-axis; the bent molecule lies in the $xy$-plane.The lowest four singlet potential energy surfaces, $S_0$ – $S_3$, and representative cuts along the surfaces (see Fig. 1*B*) are shown in Figs. *S4* – *S5*. The lowest doublet potential curves of the cation are shown in Fig. *S6*.

Analysis of the transition dipole moments shows that the transition to the lowest ($S_1$, $\widetilde{A}^1A_2$) electronic state is strictly forbidden at all geometries (including symmetrically stretched and bent configurations), while the transition to the $S_2$ ($\widetilde{B}^1B_2$) electronic state is forbidden at linear geometries but (weakly) allowed at bent and symmetrically stretched geometries. We therefore consider for our quantum dynamical calculations only the ground ($S_0$, $\widetilde{X}^1\Sigma_g^+$) and the second excited ($S_2$, $\widetilde{B}^1B_2$) electronic states, the corresponding permanent dipole moments of these electronic states and the transition dipole moment coupling them.

From these results, we already conclude that at 180° (linear geometry), no transition to any of the lower-lying excited electronic states can occur. However, the transition only becomes possible if the molecule bends and stretches, enabling a transition to only this particular $S_2$ electronic state (*i.e.*, our $\widetilde{B}^1B_2$ state).

**E. Quantum Dynamical Wave Packet Calculations.** Dynamics calculations have been performed by numerically integrating the time-dependent Schrödinger equation on a $1024 \times 512$ grid (in $R$ and $\Phi$) for the two Born-Oppenheimer electronic surfaces $\widetilde{X}^1\Sigma_g^+$ and $\widetilde{B}^1B_2$, coupled *via* dipole interaction:

$$i\hbar\frac{\partial}{\partial t}\begin{pmatrix}\chi_{\widetilde{X}}(R,\Phi,t)\\ \chi_{\widetilde{B}}(R,\Phi,t)\end{pmatrix} = \left[\begin{pmatrix}\hat{T}0\\ 0\hat{T}\end{pmatrix} + \begin{pmatrix}V_{\widetilde{X}}(R,\Phi) - \vec{\mu}_{\widetilde{X}}(R,\Phi)\vec{E}(t) & -\vec{\mu}_{\widetilde{X}\to\widetilde{B}}(R,\Phi)\vec{E}(t)\\ -\vec{\mu}_{\widetilde{X}\to\widetilde{B}}(R,\Phi)\vec{E}(t) & V_{\widetilde{B}}(R,\Phi) - \vec{\mu}_{\widetilde{B}}(R,\Phi)\vec{E}(t)\end{pmatrix}\right]\begin{pmatrix}\chi_{\widetilde{X}}(R,\Phi,t)\\ \chi_{\widetilde{B}}(R,\Phi,t)\end{pmatrix}. \tag{S6}$$

In the above equation, $\hat{T}$ is the kinetic energy operator, given by

$$\hat{T} = \left(\frac{\rho_R^2}{2M_{CS}} + \frac{\rho_\Phi^2}{2M_{SCS}}\right), \tag{S7}$$

with a mass $M_{CS}$ = 13.3142 amu used for stretching and $M_{SCS}$ = 31.9721 amu for the bending motion. By doing so, we neglect the small dependence of the mass $M_{SCS}$ on the bending angle $\Phi$. The time-dependent nuclear wave functions $\chi_i(R,\Phi,t)$ describe the field-driven vibrational wave packet dynamics in the electronic states $i$ = $\widetilde{X}$, $\widetilde{B}$. We account for the relative orientation of the molecule relative to the laser polarization direction through the angle $\theta$, defined such that

$$\tan\theta = \frac{\mu_y}{\mu_x}, \tag{S8}$$

for molecules lying in the $xy$-plane. The laser field, $E(t)$, is described classically as

$$E(t) = E_0 f(t - t_c)\cos(\omega t), \tag{S9}$$

where $E_0$ is the laser field strength, $f(t - t_c)$ is the Gaussian envelope function centered around $t_c$, and $\omega$ is the laser frequency. For these quantum dynamical calculations, we use the split-operator method (25), while the Fourier transform is done numerically using the FFTW3 library (26). In order to avoid grid reflections, absorbing boundary conditions are employed along the C-S stretching coordinate $R_{CS}$.

We have performed three different calculations for θ = 0°, 45° and 90°. Our wave packet calculations of the neutral $CS_2$ molecule show that upon interaction with the intense laser field, the electronic ground state, $\widetilde{X}^1\Sigma_g^+$, of the $CS_2$ molecule is strongly re-shaped (see Fig. 3*A*). Consequently, the field-free vibrational ground state is not an eigenstate of the field-dressed potential curve, as the potential is modified in the field. Thus, a vibrational wave packet is formed, and the molecule in its electronic ground state starts to slightly stretch to approximately $R_{CS}$ = 1.7 Å and then begins to bend up to 170° (see Fig. 4*A*).

Then, almost transiently, a small amount of population is transferred to the $\widetilde{B}^1B_2$ excited state, which immediately starts to propagate on the field-dressed potential energy surface of the $\widetilde{B}^1B_2$ state (Figs. 3*A* and 3*B*). As to be expected when considering the transition dipole moments and their components, the transition for 0° (along the y-axis, which is the molecular axis, see above) is largest, while the out-of-plane transition (along the $z$-axis) is negligible. These quantum dynamical calculations show that the wave packet in the excited state bends up to about 120° at around the peak of the laser pulse envelope (*i.e. t* = 0 fs in Fig. 4*A*) where the field is strongest, and thus, the tunneling rate reaches a maximum. As we cannot properly describe ionization with the quantum dynamical calculations (transition dipole moments from the neutral to the cation are not accounted for here), we separately calculate the dynamics of the cation.

For the cation, we have performed field-free Born-Oppenheimer-type calculations on a few lowest-lying potential energy surfaces in order to estimate the dynamical timescales imprinted during the excursion of the liberated electron until its return (within ∼8 fs), when it diffracts against the cation. The results are shown in Fig. 4*B*. We conclude that in all of the eight lowest-lying states considered, an initially stretched and bent neutral $CS_2$ can, in the time interval between ionization and probing by the returning LIED electron 8 fs later, further stretch and bend by $\Delta R_{CS} \approx 0.1$ Å and $\Delta\Phi_{SCS} \approx 10°$, depending on the electronic state of the cation $CS_2^+$ that is populated.

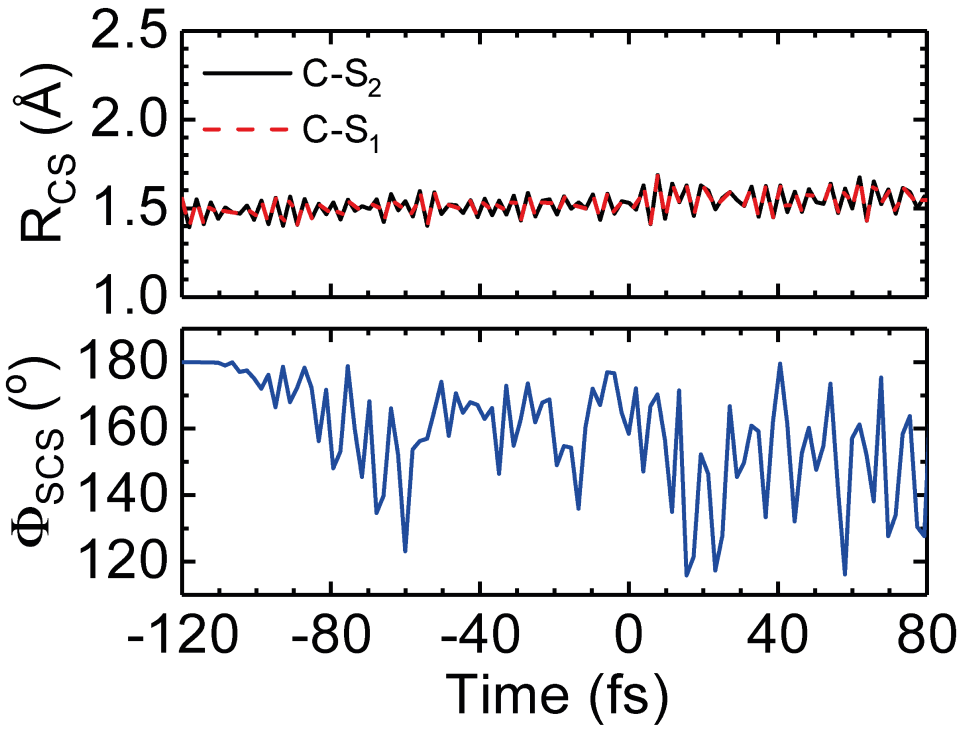


**Fig. S1 | Nuclear dynamics of $CS_2$ in the presence of a 3.1 μm laser field.** Time-dependent coordinate expectation values of the individual C-S bond lengths (*Top*), $R_{CS}$, and the S-C-S bending angle (*Bottom*), $\Phi_{SCS}$, as extracted from our real-time, real-space TDDFT calculations with moving nuclei within the Ehrenfest approach. The case for perpendicular orientation of the laser polarization axis relative to the molecular axis ($\theta$ = 90°) is shown. The same laser parameters as in the LIED measurement are used. Symmetric stretching motion mainly occurs accompanied by strong deviations from the linear geometry. Here, $t$ = 0 fs corresponds to the peak of the 85 fs (FWHM) 3.1 μm pulse envelope.

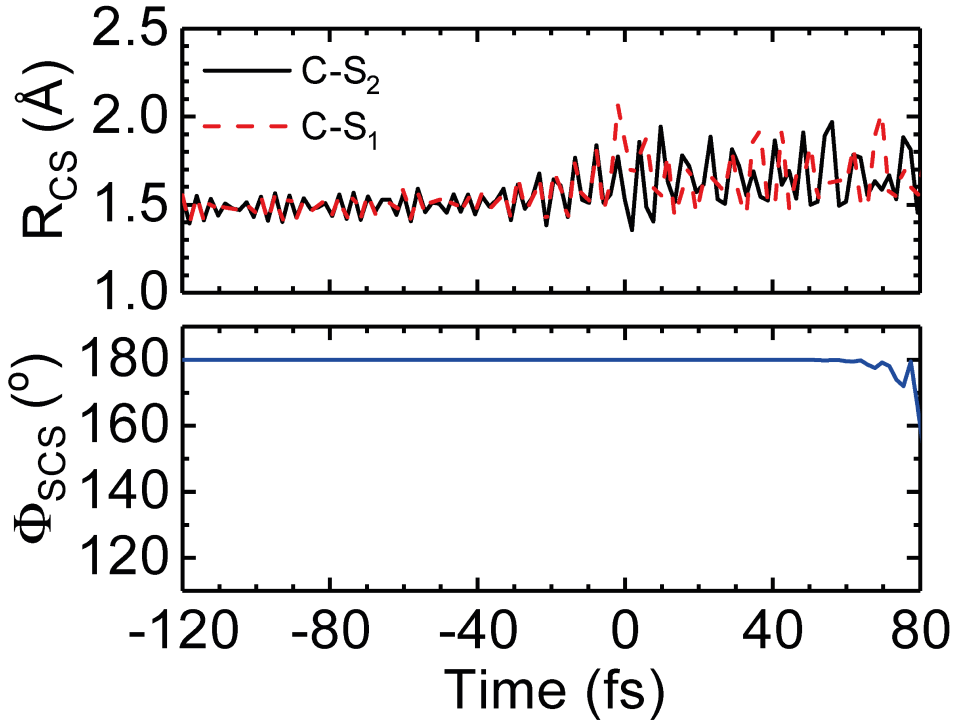


**Fig. S2 | Nuclear dynamics of $CS_2$ in the presence of a 3.1 μm laser field.** Same as in Figure *S1*, but for parallel orientation of the laser polarization axis relative to the molecular axis ($\theta = 0°$). For times $t < 0$ fs, mostly symmetric stretching dynamics can be observed, while for $t > 0$ fs antisymmetric stretching motion dominates.

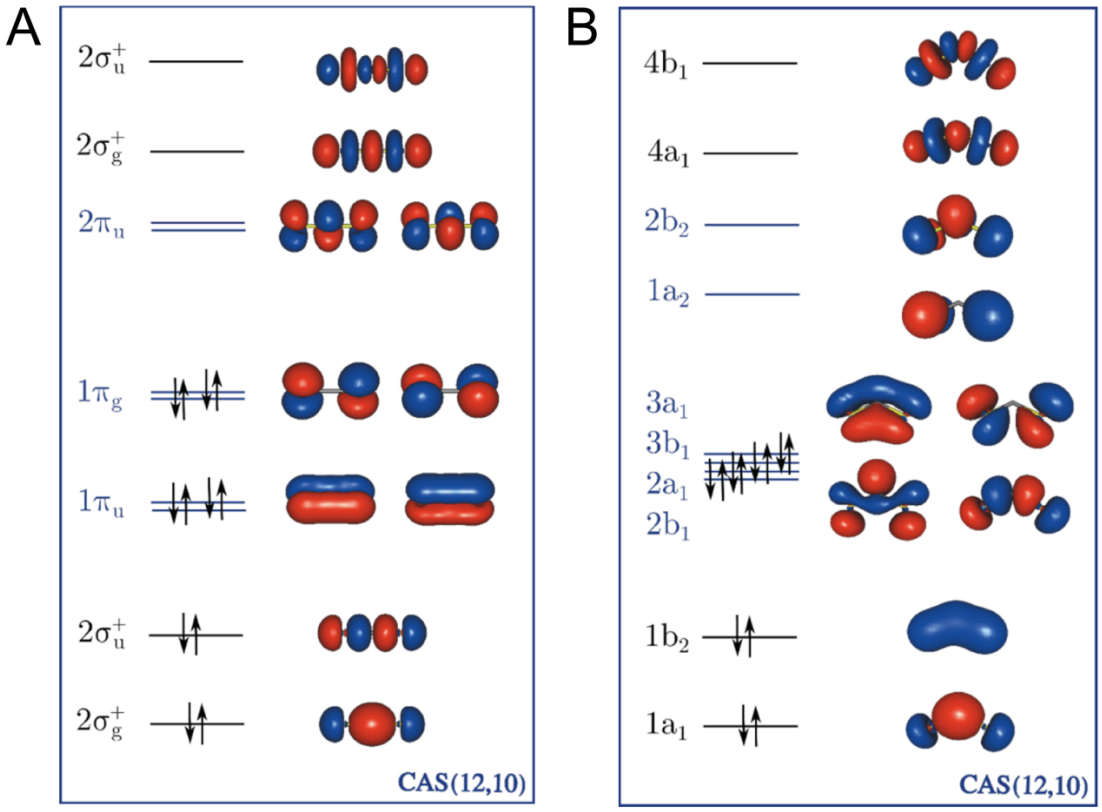


**Fig. S3 | Molecular orbitals of neutral $CS_2$.** (A) linear and (B) bent geometries chosen for the active space, showing the corresponding symmetry levels. We use a CAS(12,10)/cc-pVTZ level of theory within the OpenMolcas 8.0 program suite (23).

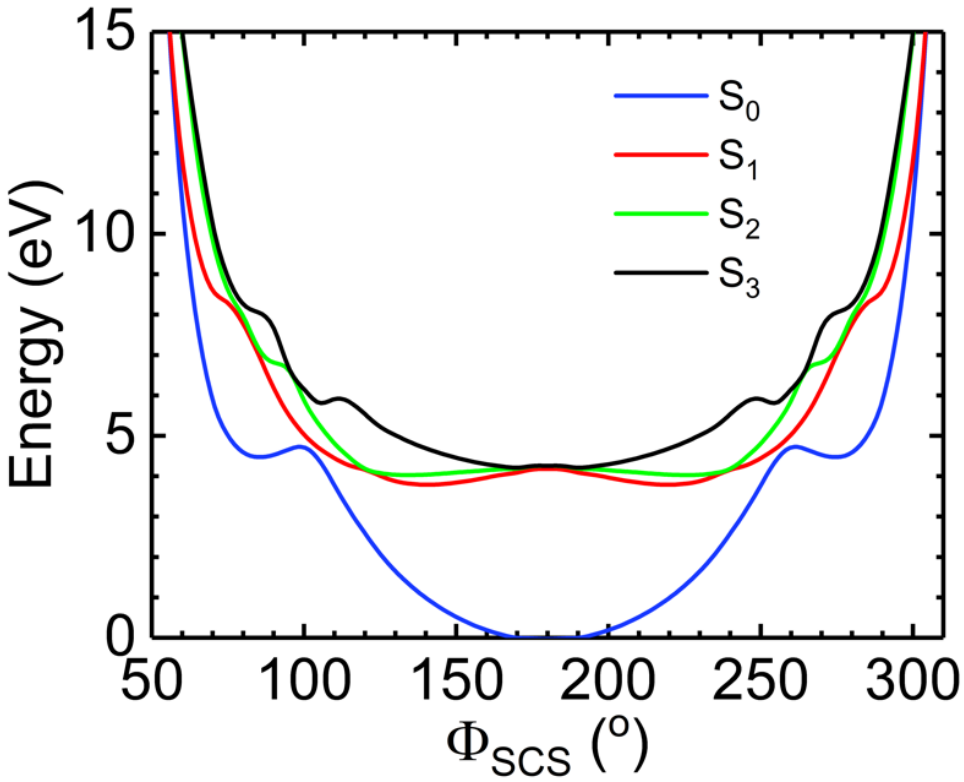


**Fig. S4 | Potential energy curves of neutral $CS_2$ along SCS bond angle coordinate.** Cut along the field-free potential energy surfaces of neutral $CS_2$ at the equilibrium C-S internuclear distance of the ground electronic state, $R_{CS}$ = 1.6 Å, showing the potential energy curves as a function of the SCS angle, $\Phi_{SCS}$, for the lowest four singlet electronic states (see labels).

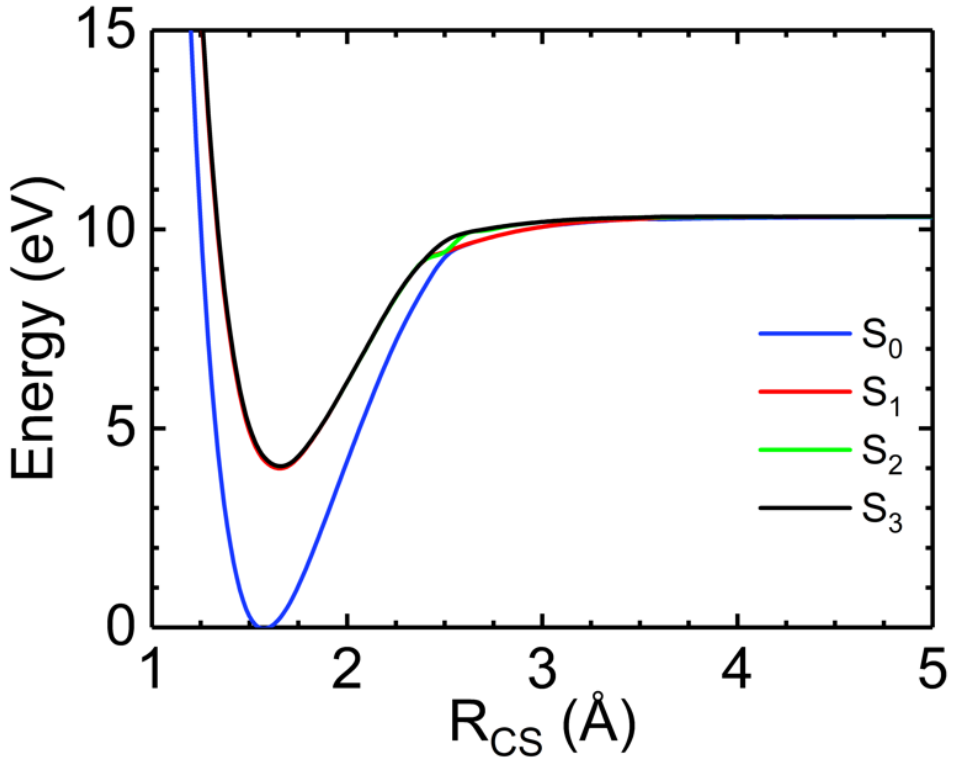


**Fig. S5 | Potential energy curves of neutral $CS_2$ along C-S internuclear distance coordinate.** Cut along the field-free potential energy surfaces of neutral $CS_2$ at the equilibrium SCS angle $\Phi_{SCS}$ = 180° showing the potential energy curves as a function of the C-S internuclear distance $R_{CS}$ of the symmetric stretch mode for the lowest four singlet electronic singlet states (see labels).

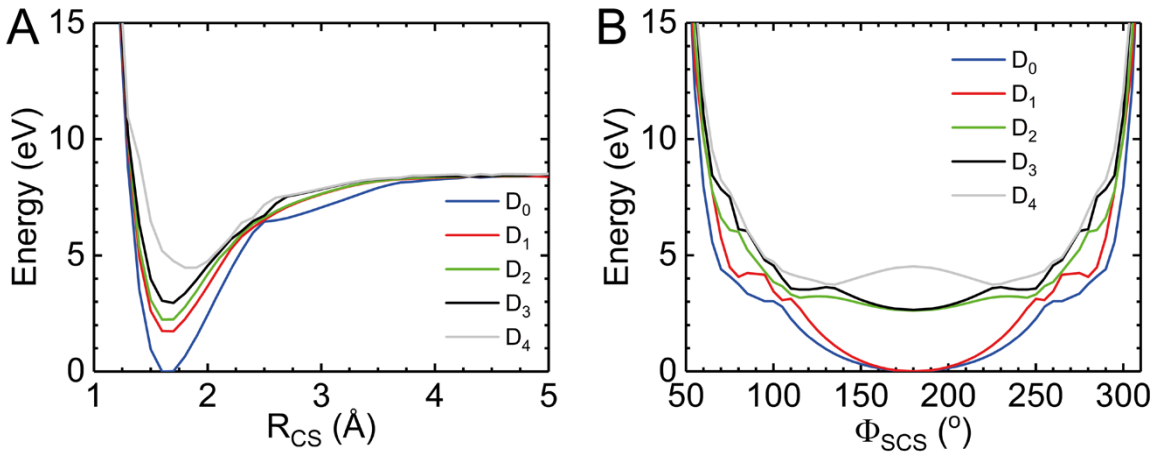


**Fig. S6 | Potential energy curves of the $CS_2^+$ cation.** (A) Cuts along the PESs of $CS_2^+$ cation at the equilibrium SCS angle $\Phi_{SCS}$ = 180° showing the potential energy curves as a function of the C-S internuclear distance $R_{CS}$ along the symmetric stretch mode. (B) Cuts along the PESs at the equilibrium C-S internuclear distance of the electronic ground state, $R_{CS}$ = 1.6 Å, showing the potential energy curves as a function of the SCS angle, $\Phi_{SCS}$, for the lowest five doublet electronic states (see labels).

**Table S1 | Field-free eigenenergies of the highest molecular orbitals (MOs) of $CS_2$ with the real-time-real-space TDDFT as implemented in the Octopus program package (17).** The energies are given in electronvolts (eV). Displayed are the results of different calculations with different functionals and self-interaction corrections, as labelled. The experimental values are taken from Eland *et al.* (22). The grey shaded LDA (adsic) calculations gave the best eigenenergies as compared to the experimental values and were the ones chosen for the following calculations when interaction with the field is included.

| MO | HF | LDA | LDA (amaldi) | LDA (adsic) | LB94 (adsic) | LB94 | LB94 (amaldi) | Expt.[22] (adsic) |
|---|---|---|---|---|---|---|---|---|
| $2\sigma_g$ | -31.2 | -21.4 | -29.0 | -24.9 | -25.7 | -33.7 | -25.3 | - |
| $2\sigma_u$ | -27.9 | -19.3 | -26.9 | -22.8 | -23.5 | -31.4 | -23.1 | - |
| $2\sigma_g$ | -18.5 | -12.7 | -19.9 | -15.9 | -17.2 | -24.8 | -16.3 | - |
| $2\sigma_u$ | -15.9 | -10.8 | -18.0 | -14.0 | -15.1 | -22.8 | -14.4 | -14.5 |
| $1\pi_g$ | -14.4 | -9.8 | -17.0 | -13.9 | -14.5 | -22.2 | -13.9 | -12.7 |
| $1\pi_g$ | -10.2 | -6.9 | -13.9 | -10.3 | -11.5 | -19.1 | -10.8 | -10.1 |

## References


1. Baudisch M, Wolter B, Pullen M, Hemmer M, Biegert J (2016) High power multi-color OPCPA source with simultaneous femtosecond deep-UV to mid-IR outputs. *Opt Lett* 41:3583-3586.

2. Elu U, *et al.* (2017) High average power and single-cycle pulses from a mid-IR optical parametric chirped pulse amplifier. *Optica* 4: 1024-1029.

3. Thai A, Hemmer M, Bates P, Chalus O, Biegert J (2011) Sub-250-mrad, passively carrier–envelope-phase-stable mid-infrared OPCPA source at high repetition rate. *Opt Lett* 36:3918-3920.

4. Ullrich J, *et al.* (2003) Recoil-ion and electron momentum spectroscopy: reaction-microscopes. *Rep Prog Phys* 66:1463.

5. Wolter B, *et al.* (2015) Strong-field physics with mid-IR fields. *Phys Rev X* 5:021034.

6. Morishita T, Le A-T, Chen Z, Lin CD (2008) Accurate retrieval of structural information from laser-induced photoelectron and high-order harmonic spectra by few-cycle laser pulses. *Phys Rev Lett* 100:013903.

7. Chen Z, Le A-T, Morishita T, Lin CD (2009) Quantitative rescattering theory for laser-induced high-energy plateau photoelectron spectra. *Phys Rev A* 79:033409.

8. Lin CD, Le A-T, Chen Z, Morishita T, Lucchese R (2010) Strong-field rescattering physics–self-imaging of a molecule by its own electrons. *J Phys B* 43:122001.

9. Xu J, Chen Z, Le A-T, Lin CD (2010) Self-imaging of molecules from diffraction spectra by laser-induced rescattering electrons. *Phys Rev A* 82:033403.

10. Pullen MG, *et al.* (2015) Imaging an aligned polyatomic molecule with laser-induced electron diffraction. *Nat Commun* 6:7262.

11. Kumarappan V, *et al.* (2008) Multiphoton electron angular distributions from laser-aligned $CS_2$ molecules. *Phys Rev Lett* 100:093006.

12. Bandrauk AD, Fowe EP (2010) Non perturbative time-dependent density functional theory, TDDFT: Study of ionization and harmonic generation in linear di-($N_2$) and tri-($CO_2$, OCS, $CS_2$) atomic molecules with ultrashort intense laser pulses-orientational effects. *Coherence and Ultrashort Pulse Laser Emission*.

13. Murai H, *et al.* (2013) A comprehensive and comparative study of elastic electron scattering from OCS and $CS_2$ in the energy region from 1.2 to 200 eV. *J Chem Phys* 138:054302.

14. Blaga CI, *et al.* (2012) Imaging ultrafastmolecular dynamicswith laser-induced electron diffraction. *Nature* 483:194.

15. Pullen MG, *et al.* (2016) Influence of orbital symmetry on diffraction imaging with rescattering electron wave packets. *Natu Commun* 7:11922.

16. Wolter B, *et al.* (2016) Ultrafast electron diffraction imaging of bond breaking in di-ionized acetylene. *Science* 354:308.

17. Andrade X, *et al.* (2015) Real-space grids and the octopus code as tools for the development of new simulation approaches for electronic systems. *Phys Chem Chem Phys* 17:31371.

18. Dirac PA (1930) Note on exchange phenomena in the Thomas atom. *Math Proc Camb Philos Soc* 26:376.

19. Bloch MF (1929) Bemerkung zur Elektronentheorie des Ferromagnetismus und der elektrischen Leitfähigkeit. *Zeitschrift für Physik* 57:545.

20. Perdew JP, Zunger A (1981) Self-interaction correction to density-functional approximations for many-electron systems. *Phys Rev B* 23:5048.

21. Legrand C, Suraud E, Reinhard P (2002) Comparison of self-interaction-corrections for metal clusters. *J Phys B* 35:1115.

22. Eland JH, Danby C (1968) Photoelectron spectra and ionic structure of carbon dioxide, carbon disulphide and sulphur dioxide. *Int J Mass Spectrom* 1:111.

23. Aquilante F, *et al.* (2016) Molcas 8: New capabilities for multiconfigurational quantum chemical calculations across the periodic table. *J Comput Chem* 37:506.

24. Woon DE, Dunning Jr TH (1995) Gaussian basis sets for use in correlated molecular calculations. V. Core-valence basis sets for boron through neon. *J Chem Phys* 103:4572.

25. Feit M, Fleck Jr J, Steiger A (1982) Solution of the schrödinger equation by a spectral method. *J Comput Phys* 47:412.

26. Frigo M, Johnson SG (1998) FFTW. *ICASSP conference proceedings* 3:1381.